

Linear–Nonlinear Fusion Neural Operator for Partial Differential Equations

Heng Wu^{1,2}, Junjie Wang^{1,2}, and Benzhuo Lu^{*1,2}

¹SKLMS, ICMSEC, NCMIS, Academy of Mathematics and Systems Science, Chinese Academy of Sciences, Beijing 100190, China

²School of Mathematical Sciences, University of Chinese Academy of Sciences, Beijing 100049, China

Abstract

Neural operator learning directly constructs the mapping relationship from the equation parameter space to the solution space, enabling efficient direct inference in practical applications without the need for repeated solution of partial differential equations (PDEs) — an advantage that is difficult to achieve with traditional numerical methods. In this work, we find that explicitly decoupling linear and nonlinear effects within such operator mappings leads to markedly improved learning efficiency. This yields a novel network structure, namely the Linear–Nonlinear Fusion Neural Operator (LNF-NO), which models operator mappings via the multiplicative fusion of a linear component and a nonlinear component, thus achieving a lightweight and interpretable representation. This linear–nonlinear decoupling enables efficient capture of complex solution features at the operator level while maintaining stability and generality. LNF-NO naturally supports multiple functional inputs and is applicable to both regular grids and irregular geometries. Across a diverse suite of PDE operator-learning benchmarks, including nonlinear Poisson–Boltzmann equations and multi-physics coupled systems, LNF-NO is typically substantially faster to train than Deep Operator Networks (DeepONet) and Fourier Neural Operators (FNO), while achieving comparable or better accuracy in most cases. On the tested 3D Poisson–Boltzmann case, LNF-NO attains the best accuracy among the compared models and trains approximately $2.7\times$ faster than a 3D FNO baseline.

1 Introduction

Neural operator learning has emerged as a central paradigm in scientific machine learning for approximating solution operators of partial differential equations (PDEs). By learning mappings between function spaces, neural operators aim to amortize the cost of repeatedly solving PDEs under varying boundary conditions, source terms, or coefficients. Such many-query settings arise ubiquitously in physical, chemical, and biological modeling, where repeated numerical solves constitute a major computational bottleneck [1, 2, 3]. Neural operators provide fast surrogate models that deliver approximate PDE solutions with accuracy often sufficient for downstream analysis and decision-making, while substantially reducing computational cost compared with repeated high-fidelity simulations [4, 5].

Among existing approaches, the Deep Operator Network (DeepONet) [4] and the Fourier Neural Operator (FNO) [6] represent the most widely used and representative neural operator models. DeepONet employs a branch–trunk decomposition to learn operator mappings from input functions to solution fields, while FNO leverages global convolution in the Fourier domain to efficiently capture long-range dependencies on regular grids. Beyond these baselines, a growing family of neural operator architectures has been proposed, including geometry-informed operators [7], multiscale U-shaped designs [8], and transformer-inspired formulations [9].

*Corresponding author. E-mail: bzlu@lsec.cc.ac.cn

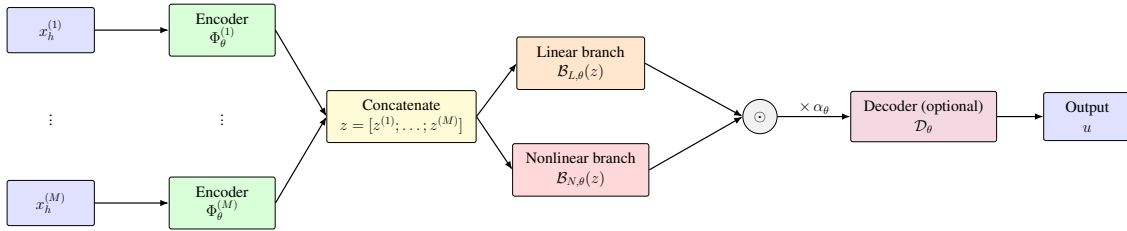


Fig. 1: Architecture of the proposed Linear–Nonlinear Fusion Neural Operator (LNF-NO). Each input component (typically a discretized function, e.g., boundary traces or source fields) is encoded separately and concatenated into a latent representation. An operator core then fuses a linear branch and a nonlinear branch via element-wise multiplication (\odot), producing a raw prediction that can be optionally refined by a lightweight decoder. Arrows indicate the data flow.

Despite this progress, several challenges remain in practical operator-learning settings. First, nonlinear interactions in PDE operators can be difficult to represent or optimize using purely additive architectural compositions. Second, many real-world problems involve *multiple functional inputs*, such as boundary traces, source terms, or coefficient fields, as well as coupled multi-field outputs. Third, training efficiency and optimization stability become increasingly important as problem complexity grows, particularly for three-dimensional PDEs and large-scale benchmarks.

Non-additive interactions have proven effective across a wide range of deep learning architectures. Feature-wise modulation mechanisms, such as Feature-wise Linear Modulation (FiLM), apply learned, input-dependent scaling to intermediate representations and can enhance expressivity with minimal computational overhead [10]. More broadly, attention mechanisms [11] and mixture-of-experts models [12] illustrate that structured, conditional interactions between multiple components can improve representational capacity and training efficiency. These developments motivate exploring multiplicative fusion as a general design principle for neural operator architectures.

Our architectural design is further motivated by numerical insights into semi-linear elliptic PDEs and coupled systems. For instance, in biomolecular electrostatics and ion transport, solutions to nonlinear equations such as Poisson–Boltzmann or Poisson–Nernst–Planck are often viewed as being predominantly governed by their corresponding linear approximations, modulated by nonlinear correction terms [13, 14]. Inspired by this, we hypothesize that explicitly disentangling these linear and nonlinear effects within the neural architecture serves as an effective physics-aware inductive bias.

In this work, we propose the Linear–Nonlinear Fusion Neural Operator (LNF-NO), which models operator behavior through the multiplicative interaction of a linear component and a nonlinear component. Crucially, LNF-NO treats these components symmetrically: the two branches interact directly through element-wise fusion, rather than being combined through hierarchical or purely additive structures. This design provides a lightweight and interpretable mechanism for capturing nonlinear effects while maintaining architectural simplicity and stable optimization behavior. LNF-NO naturally supports multiple functional inputs by encoding each input function independently and fusing their latent representations within the operator core. The architecture can be paired with a lightweight grid-based decoder for standard benchmark problems, or used in a decoder-free setting for irregular geometries where solutions are predicted at sampled points.

We evaluate LNF-NO on a diverse suite of PDE operator-learning benchmarks, including nonlinear Poisson–Boltzmann equations, coupled multi-field systems, and domains with irregular geometries. Across these tasks, LNF-NO consistently improves training efficiency relative to widely used baselines, while achieving comparable accuracy in most cases. In particular, we present a three-dimensional Poisson–Boltzmann case study in which LNF-NO attains lower error than a 3D FNO while requiring noticeably less training time.

The main contributions of this work are summarized as follows:

- We introduce a linear–nonlinear multiplicative fusion mechanism that explicitly decouples complementary effects. This design acts as an efficiency-oriented inductive bias, yielding significantly improved training efficiency (e.g., $2.7\times$ speedup on 3D tasks) compared to spectral baselines, while achieving

comparable or improved accuracy in most cases.

- Our simple and flexible architecture naturally accommodates multiple functional inputs and predicts multiple coupled output fields within a unified framework, seamlessly generalizing across both regular grids and irregular geometries without task-specific modifications.
- We demonstrate the scalability and robustness of LNF-NO on a diverse suite of benchmarks, including three-dimensional systems and strongly nonlinear equations (e.g., Poisson–Boltzmann), effectively capturing complex dynamics where standard baselines often face computational or stability bottlenecks.

2 Methodology

2.1 Operator learning with input/output discretization

Let $\mathcal{G} : \mathcal{X} \rightarrow \mathcal{Y}$ denote the solution operator of a PDE posed on a bounded domain $\Omega \subset \mathbb{R}^d$, mapping input functions (e.g., boundary traces, coefficient fields, or source terms) to solution fields. In practice, operator learning is carried out after discretizing *both* inputs and outputs.

Input discretization. We consider *multi-function* inputs with M components

$$x = (x^{(1)}, \dots, x^{(M)}), \quad x^{(m)} \in \mathcal{X}^{(m)}.$$

Each component is discretized by a sampling or projection operator $\mathcal{I}_h^{(m)} : \mathcal{X}^{(m)} \rightarrow \mathbb{R}^{d_{\text{in}}^{(m)}}$, yielding $x_h^{(m)} := \mathcal{I}_h^{(m)}(x^{(m)})$. Stacking all components gives $x_h := \mathcal{I}_h(x) \in \mathbb{R}^{d_{\text{in}}}$, where $d_{\text{in}} = \sum_{m=1}^M d_{\text{in}}^{(m)}$. In general, \mathcal{I}_h is not invertible.

Data-generating family and lifting. The dataset is generated from a restricted family $\mathcal{A} \subset \mathcal{X}$. Accordingly, we only require the discrete learning target to be well defined on the set of discrete inputs observed in data. Let $K_h := \mathcal{I}_h(\mathcal{A}) \subset \mathbb{R}^{d_{\text{in}}}$. We fix a (possibly non-unique) selection map $\mathcal{L}_h : K_h \rightarrow \mathcal{A}$ such that $\mathcal{I}_h(\mathcal{L}_h(x_h)) = x_h$ for all $x_h \in K_h$. The choice of \mathcal{L}_h reflects the data-generation procedure and does not require uniqueness.

Output discretization. Let $\mathcal{I}_h^{\text{out}} : \mathcal{Y} \rightarrow \mathbb{R}^{d_{\text{out}}}$ denote an output sampling or projection map, such as evaluation on a fixed grid or a fixed point set for irregular domains. For C_{out} output fields, typically $d_{\text{out}} = C_{\text{out}} N_{\text{out}}$.

Discrete target operator. We define the discrete operator learning target

$$F_h^* := \mathcal{I}_h^{\text{out}} \circ \mathcal{G} \circ \mathcal{L}_h, \quad F_h^* : K_h \rightarrow \mathbb{R}^{d_{\text{out}}}. \quad (1)$$

All models are trained and evaluated in the discrete output space $\mathbb{R}^{d_{\text{out}}}$.

2.2 LNF-NO architecture (multi-input, multi-output)

Fig. 1 overviews the LNF-NO architecture, generally formulated to handle multiple functional inputs (e.g., boundary conditions and source terms) and predict multiple coupled output fields (multi-output). Given $x_h = (x_h^{(1)}, \dots, x_h^{(M)})$, each input component is encoded independently:

$$\begin{aligned} z^{(m)} &= \Phi_\theta^{(m)}(x_h^{(m)}) \in \mathbb{R}^{d_m}, \quad m = 1, \dots, M, \\ z &= [z^{(1)}; \dots; z^{(M)}] \in \mathbb{R}^{d_z}. \end{aligned}$$

The operator core consists of a linear branch and a nonlinear branch fused multiplicatively:

$$u_{\text{raw}} = \alpha_\theta \cdot (\mathcal{B}_{L,\theta}(z) \odot \mathcal{B}_{N,\theta}(z)) \in \mathbb{R}^{d_{\text{out}}}, \quad (2)$$

where \odot denotes element-wise multiplication and α_θ is a learnable scalar (see Appendix C for initialization details). Both branches map the latent representation to the discrete output space, $\mathcal{B}_{L,\theta}, \mathcal{B}_{N,\theta} : \mathbb{R}^{d_z} \rightarrow \mathbb{R}^{d_{\text{out}}}$, with $\mathcal{B}_{L,\theta}$ being affine and $\mathcal{B}_{N,\theta}$ a nonlinear MLP.

Remark. In practice, performance reflects both structured feature extraction (e.g., convolutional encoders/decoders on grids) and the lightweight multiplicative fusion in (2). As shown in Appendix D, strong accuracy can be achieved even with simplified operator cores, highlighting the role of the encoder–decoder pipeline as an additional inductive bias.

Intuition. The proposed fusion strategy is conceptually grounded in both numerical analysis and deep learning. Physically, the explicit decoupling of the operator into linear and nonlinear branches mirrors operator decomposition strategies inspired by numerical practices and empirical insights (see, e.g., [13] for Poisson–Boltzmann and [14] for Poisson–Nernst–Planck, where solutions are often globally close to their linear counterparts). Structurally, in contrast to additive compositions such as residual connections in ResNets [15] which learn corrections via summation, our multiplicative fusion allows the nonlinear branch to spatially gate or scale this dominant linear baseline in an input-adaptive manner. This parallels feature-wise modulation mechanisms (e.g., FiLM [10]) but is explicitly formulated to capture the coupled linear–nonlinear nature of PDE operators.

Optionally, a lightweight decoder \mathcal{D}_θ refines local consistency on regular grids:

$$F_\theta(x_h) = \begin{cases} u_{\text{raw}}, & \text{decoder-free,} \\ \mathcal{D}_\theta(u_{\text{raw}}), & \text{with decoder.} \end{cases}$$

2.3 Approximation Guarantee

Theorem 2.1 (Universal approximation). *Assume $K_h \subset \mathbb{R}^{d_{\text{in}}}$ is compact and $F_h^* \in C(K_h; \mathbb{R}^{d_{\text{out}}})$. If LNF-NO employs non-polynomial activations (e.g., ReLU or tanh) in its feedforward components, then for any $\varepsilon > 0$ there exist parameters θ such that*

$$\sup_{x_h \in K_h} \|F_\theta(x_h) - F_h^*(x_h)\| \leq \varepsilon.$$

Proof sketch. By selecting encoder and decoder parameters so that they reduce to identity mappings (or fixed linear embeddings) on K_h , and setting $\mathcal{B}_{L,\theta}(z) \equiv \mathbf{1}$ and $\alpha_\theta = 1$, the architecture contains a standard feedforward network from $\mathbb{R}^{d_{\text{in}}}$ to $\mathbb{R}^{d_{\text{out}}}$ as a special case. Universal approximation then follows from classical results for non-polynomial activations [16, 17]. \square

2.4 Optimization

We train LNF-NO by supervised learning on pairs (x_h, y_h) with $y_h = F_h^*(x_h)$. We use the averaged relative ℓ_2 error across output fields as the loss:

$$\mathcal{L}(\theta) = \frac{1}{B} \sum_{b=1}^B \frac{1}{C_{\text{out}}} \sum_{c=1}^{C_{\text{out}}} \frac{\|\hat{y}_{h,b}^{(c)} - y_{h,b}^{(c)}\|_2}{\|y_{h,b}^{(c)}\|_2 + \varepsilon}. \quad (3)$$

All losses and metrics are computed on the decoded physical scale after inverse normalization. We optimize using AdamW [18] with a fixed learning rate (see Appendix for full hyperparameters). Following common practice, we exclude bias terms and the scalar fusion scale α_θ from weight decay, since they act as calibration parameters rather than capacity-controlling weights.

3 Results

Unified protocol. All models are trained and evaluated under a unified experimental protocol. For each task, we use identical training and test sets across all methods with a fixed 9:1 split, and report the mean relative ℓ_2 error on the test set. DeepONet is trained with a learning rate of 10^{-4} (except for Navier–Stokes, which uses 2.5×10^{-4}) for 5000 epochs, while FNO and LNF-NO are trained with a learning rate of 10^{-3} (except for Navier–Stokes, which uses 2.5×10^{-3}) for 500 epochs, reflecting their faster convergence and

stable optimization at larger step sizes. Training time is measured on the same hardware and includes the full training process. Additional implementation details, including architectures per task, solver settings, and data generation procedures, are provided in the appendix.

Task definitions. In all benchmarks, we learn solution operators that map boundary conditions and/or input fields to solution fields evaluated on a fixed set of points. We summarize the PDE tasks considered in this work below.

Laplace. We study the 2D Laplace equation $\Delta u = 0$ in $\Omega = (0,1)^2$ with Dirichlet boundary condition $u|_{\partial\Omega} = g$, and learn the operator mapping the boundary trace g to the solution field u on a fixed grid (see Appendix A.1).

Burgers. We consider the 1D viscous Burgers equation

$$\partial_t u + u \partial_x u = \nu \partial_{xx} u \quad \text{on } x \in [0, 2\pi), t \in [0, T], \quad (4)$$

with periodic boundary conditions. The operator maps the initial condition $u(\cdot, 0)$ to the solution trajectory $u(\cdot, t)$ on a fixed space–time grid (see Appendix A.2).

Darcy flow. We benchmark the elliptic Darcy equation $-\nabla \cdot (a(x)\nabla u) = f$ in $\Omega = (0,1)^2$, where $a(x)$ denotes the permeability field. Both smooth and piecewise constant permeability regimes are considered (see Appendix A.3).

Poisson–Boltzmann (PB). We evaluate the nonlinear Poisson–Boltzmann operator

$$-\Delta u + k \sinh(u) = f \quad \text{in } \Omega, \quad u|_{\partial\Omega} = g, \quad (5)$$

where $k > 0$ partially controls the strength of the nonlinearity. The source-free case corresponds to $f = 0$, while the source-driven case uses $f \neq 0$ (see, e.g., [13] for background on numerical PB models and Appendix A.4 for benchmark details).

Irregular-domain PB. To evaluate geometric generalization, we further consider source-free PB problems posed on irregular planar domains with multiple boundary components, discretized using finite element methods and represented in a node-based format (see Appendix A.4.3).

Navier–Stokes. We consider the two-dimensional incompressible Navier–Stokes equations in vorticity form, which implicitly enforces the divergence-free condition:

$$\partial_t \omega + \mathbf{u} \cdot \nabla \omega = \nu \Delta \omega + f, \quad \mathbf{u} = \nabla^\perp \psi, \quad \Delta \psi = \omega. \quad (6)$$

The operator maps the initial vorticity field $\omega(\cdot, 0)$ to $\omega(\cdot, t)$ at prescribed time snapshots on a fixed grid.

Poisson–Nernst–Planck (PNP). Finally, we benchmark a multi-field coupled operator corresponding to the Poisson–Nernst–Planck system (see, e.g., [14] for the classical PNP formulation and Appendix A.6 for dataset details). A dimensionless form is taken where physical parameters are set to unity for operator-learning purposes:

$$-\Delta \phi = c_+ - c_-, \quad \nabla \cdot (\nabla c_\pm \pm c_\pm \nabla \phi) = 0. \quad (7)$$

The operator maps boundary traces to the electric potential ϕ and ion concentration fields c_\pm on a fixed grid.

3.1 Baseline benchmarks on regular grids

3.1.1 Single-input operators

We first consider standard *single-input* operator-learning benchmarks on regular grids, including Laplace, Burgers, Darcy flow (smooth and discontinuous coefficients), source-free Poisson–Boltzmann ($k = 1$), and Navier–Stokes equations. These tasks span linear and nonlinear elliptic and parabolic operators with varying degrees of complexity.

The quantitative results are summarized in Table 1. As shown in the table, LNF-NO consistently requires substantially less wall-clock training time than DeepONet across all benchmarks (e.g., roughly $10\times$ faster on Laplace). Compared with FNO, LNF-NO is typically faster to train while achieving comparable accuracy on most tasks. For instance, on the Darcy flow (Smooth) benchmark, LNF-NO achieves an error of 3.39×10^{-3} ,

Table 1: Baseline benchmarks on regular grids (single-input operators). We report the test mean relative ℓ_2 error and wall-clock training time under the unified protocol.

EQUATION	MODEL	#PARAMS	EPOCHS	TRAINING TIME (s)	TEST REL. L2
LAPLACE	DEEPONET	973,313	5000	1470.08	1.16E-02
	FNO	9,133,866	500	999.22	1.66E-02
	LNF-NO	2,343,700	500	139.38	1.11E-02
BURGERS	DEEPONET	938,497	5000	1760.09	1.05E-01
	FNO	8,413,953	500	2316.45	1.20E-02
	LNF-NO	3,767,618	500	509.37	3.86E-02
DARCY (SMOOTH COEFF.)	DEEPONET	5,182,209	5000	4981.13	5.65E-02
	FNO	8,413,953	500	3889.17	2.58E-03
	LNF-NO	5,389,412	500	283.56	3.39E-03
DARCY (PIECEWISE COEFF.)	DEEPONET	15,790,849	5000	36945.35	4.87E-02
	FNO	8,413,953	500	11127.40	1.24E-02
	LNF-NO	75,997,220	500	1760.75	3.30E-02
PB ($k = 1$)	DEEPONET	1,024,513	5000	1685.50	6.89E-02
	FNO	11,138,266	500	3700.89	8.29E-02
	LNF-NO	7,069,300	500	465.43	2.29E-02
NAVIER-STOKES	DEEPONET	3,543,809	5000	35754.94	2.32E-01
	FNO	22,123,337	500	33563.46	5.98E-03
	LNF-NO	23,330,665	500	6511.85	4.96E-02

which is competitive with FNO’s 2.58×10^{-3} , but with significantly reduced training time (283s vs. 3889s). We note that on problems with strong spectral structure, such as Navier–Stokes, FNO benefits from its explicit Fourier inductive bias and attains lower errors, whereas LNF-NO trades part of this domain-specific accuracy for broader applicability and improved training efficiency.

3.1.2 Multi-input operators

We next consider *multi-input* operator-learning problems, where the input consists of multiple function-valued components. These include a source-driven Poisson–Boltzmann equation and a coupled Poisson–Nernst–Planck system.

Table 2 presents the performance on these multi-input tasks. LNF-NO naturally accommodates multi-function inputs through independent encoders and a shared operator core. As reported in the table, for the source-driven PB equation, LNF-NO outperforms both DeepONet and FNO in accuracy (1.91×10^{-2} vs. 3.71×10^{-2} for FNO) while being approximately $6\times$ faster than FNO. For the coupled PNP system, LNF-NO achieves accuracy comparable to FNO (2.40×10^{-2} vs. 2.21×10^{-2}) and remains substantially more efficient than DeepONet.

3.2 Nonlinear Strength Regimes in Poisson–Boltzmann Equations

We further investigate robustness under increasing nonlinearity using the source-free Poisson–Boltzmann equation with $k = 0.01, 1, \text{ and } 100$. As k increases, the operator becomes increasingly stiff and exhibits sharp boundary layers.

The results under varying nonlinearity strengths are detailed in Table 3. Across all regimes ($k = 0.01$ to 100), LNF-NO maintains stable optimization and consistently low errors (around 2% relative error). In

Table 2: Baseline benchmarks on regular grids (multi-input operators). Each task takes multiple function-valued inputs (e.g., boundary traces and a source field) and predicts fields on a fixed grid.

EQUATION	MODEL	#PARAMS	EPOCHS	TRAINING TIME (s)	TEST REL. L2
PB WITH SOURCE ($k = 1$)	DEEPONET	4,096,769	5000	2549.46	2.64E-01
	FNO	11,138,330	500	3751.44	3.71E-02
	LNF-NO	8,145,940	500	607.04	1.91E-02
PNP SYSTEM	DEEPONET	1,841,667	5000	12299.65	6.01E-02
	FNO	8,409,987	500	8197.63	2.21E-02
	LNF-NO	32,392,906	500	1799.65	2.40E-02

Table 3: Strongly nonlinear Poisson–Boltzmann regimes (source-free). We vary the nonlinearity strength k in (5) with $f = 0$ and report test mean relative ℓ_2 error and training time.

EQUATION	MODEL	#PARAMS	EPOCHS	TRAINING TIME (s)	TEST REL. L2
PB ($k = 0.01$)	DEEPONET	1,024,513	5000	1821.46	5.72E-02
	FNO	11,138,266	500	3747.64	6.24E-02
	LNF-NO	7,069,300	500	433.81	1.83E-02
PB ($k = 1$)	DEEPONET	1,024,513	5000	1685.50	6.89E-02
	FNO	11,138,266	500	3700.89	8.29E-02
	LNF-NO	7,069,300	500	465.43	2.29E-02
PB ($k = 100$)	DEEPONET	1,024,513	5000	2280.09	1.01E-01
	FNO	11,138,266	500	3735.93	1.01E-01
	LNF-NO	7,069,300	500	436.57	2.42E-02

contrast, as shown in the bottom rows of Table 3, both DeepONet and FNO exhibit degraded accuracy or significantly higher training costs as nonlinearity strengthens. For the stiffest case ($k = 100$), LNF-NO achieves a relative error of 2.42×10^{-2} , significantly outperforming both DeepONet (1.01×10^{-1}) and FNO (1.01×10^{-1}), suggesting that the proposed multiplicative fusion provides an effective inductive bias for stiff nonlinear operators.

3.3 Irregular geometries

Table 4 compares the performance on three non-rectangular geometries. LNF-NO achieves accuracy comparable to or better than DeepONet (e.g., 2.89×10^{-2} on the Star domain) while requiring roughly $7 \times$ less wall-clock training time. Crucially, these results highlight the geometric generality of our method: LNF-NO remains directly applicable on irregular domains discretized by unstructured nodes, whereas grid-based spectral operators such as FNO are not directly applicable in this setting.

3.4 Extension to three-dimensional problems

Quantitative comparisons for the 3D benchmark are provided in Table 5. LNF-NO achieves the lowest error (4.26×10^{-2}) among the compared methods and is markedly more efficient than 3D FNO (2748s vs. 7559s). Qualitatively, Figure 2 visualizes the central cross-sections of the predicted solution field $u(x, y, z)$, demonstrating that LNF-NO can accurately reconstruct the 3D potential distribution from boundary data.

Taken together, the experimental results across Tables 1–5 show a consistent pattern. On regular-grid baselines (Tables 1 and 2), LNF-NO achieves competitive accuracy while substantially reducing wall-clock

Table 4: Performance on irregular domains for the Poisson–Boltzmann equation. The problems are posed on non-rectangular geometries with complex boundaries and discretized using unstructured node-based representations, for which grid-based spectral operators such as FNO are not directly applicable.

GEOMETRY	MODEL	#PARAMS	EPOCHS	TRAINING TIME (s)	TEST REL. L2
	DEEPONET	973,313	5000	1050	3.47E-02
	LNF-NO	1,364,439	500	144	2.89E-02
	DEEPONET	973,313	5000	925	3.46E-02
	LNF-NO	1,343,879	500	152	3.53E-02
	DEEPONET	973,313	5000	1025	3.20E-02
	LNF-NO	2,158,055	500	102	3.41E-02

Table 5: Results on the 3D Poisson–Boltzmann benchmark on a 33^3 grid. We report test mean relative ℓ_2 error and wall-clock training time under the unified protocol.

MODEL	#PARAMS	EPOCHS	TIME (s)	REL. L2
DEEPONET	2.5M	5000	1348	3.34E-01
FNO (3D)	15.0M	500	7559	7.71E-02
LNF-NO	21.7M	500	2748	4.26E-02

training time compared with DeepONet, and it is often faster than FNO with comparable errors on most tasks. For problems that strongly match spectral inductive biases (e.g., periodic Navier–Stokes), FNO attains the lowest error, which is expected given its explicit Fourier structure.

Beyond regular grids, as evidenced in Table 4, LNF-NO remains directly applicable to irregular geometries represented by unstructured nodes, where grid-based spectral operators are not readily usable. In addition, on the 3D Poisson–Boltzmann benchmark (Table 5 and Fig. 2), LNF-NO maintains stable optimization and achieves lower error than the compared baselines, while being markedly more efficient than 3D FNO in wall-clock time.

Overall, these results suggest that the proposed multiplicative fusion functions primarily as an efficiency-oriented inductive bias that is broadly compatible with heterogeneous inputs, non-rectangular geometries, and three-dimensional extensions, rather than a task-specific architectural specialization. To better understand the roles of different architectural components and to disentangle the contributions of the encoders, decoder, and multiplicative operator core, we conduct systematic ablation studies reported in Appendix D.

4 Discussion

The experimental results indicate that, within the scope of the problem settings and equations investigated, LNF-NO offers a valuable trade-off between efficiency, versatility, and accuracy. Rather than claiming superiority across all possible PDE learning tasks, we position LNF-NO as a streamlined, broadly applicable framework that is particularly effective for multi-physics and geometric variations where specialized spectral baselines may face limitations.

First, LNF-NO exhibits a high degree of architectural uniformity. While grid-based spectral approaches (e.g., FNO) are inherently restricted to regular meshes and require specific adaptations for complex geometries, LNF-NO employs a unified linear–nonlinear fusion core across regular grids, irregular meshes, and three-dimensional domains. Although point-based baselines like DeepONet also support irregular geometries, our experiments on the 3D Poisson–Boltzmann benchmark suggest that they may face convergence difficulties in higher-dimensional or stiff nonlinear settings. In contrast, LNF-NO maintains stable optimiza-

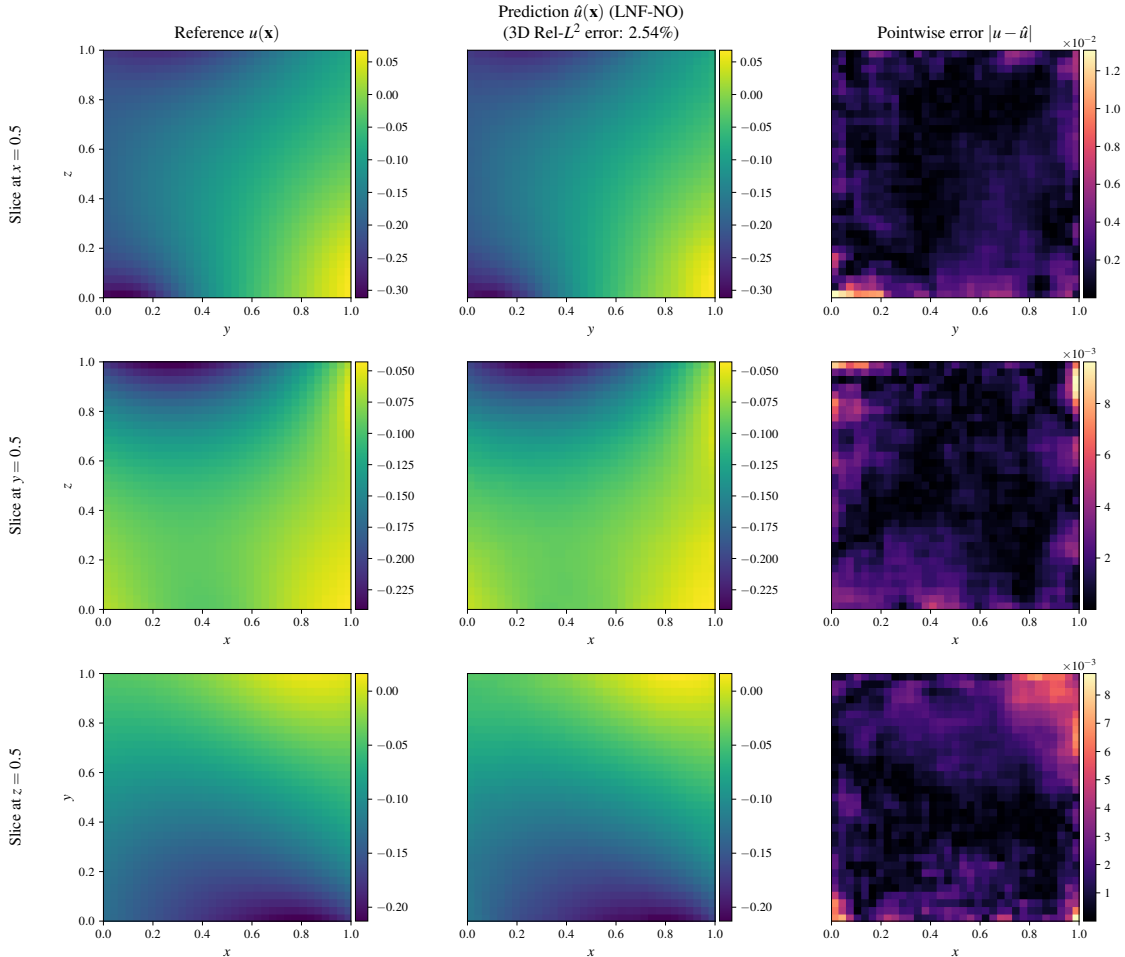


Fig. 2: 3D Poisson–Boltzmann extension. Central cross-sections of the solution field $u(x, y, z)$ at $x = 0.5$, $y = 0.5$, and $z = 0.5$. The prediction is reconstructed from boundary data by LNF-NO.

tion and consistent performance across these diverse scenarios using a single architectural paradigm. This design naturally accommodates multiple functional inputs and coupled multi-field outputs without requiring problem-specific architectural redesign.

Second, LNF-NO consistently demonstrates significantly improved training efficiency. Under a unified experimental protocol, our method requires substantially less wall-clock training time than DeepONet across all benchmarks. The multiplicative fusion structure acts as an efficiency-oriented inductive bias, accelerating convergence particularly in stiff nonlinear regimes. Unlike emerging Transformer-based large-scale foundation models [9] that prioritize massive model capacity and often incur high computational costs, LNF-NO targets an explicitly efficiency-oriented design regime. This makes it particularly suitable as a lightweight baseline for rapid exploration and analysis.

Third, regarding predictive performance, LNF-NO achieves comparable or improved accuracy in most cases relative to the baselines. It performs particularly well on strongly nonlinear elliptic problems and coupled systems. We acknowledge that for problems dominated by global transport with periodic boundaries, such as Navier–Stokes, Fourier-based operators benefit from their explicit spectral inductive bias and attain lower errors. However, LNF-NO provides reasonable approximations in these settings while offering superior training speed and broader geometric applicability.

Future work will focus on extending the fusion mechanism to practical engineering contexts involving

more complex geometries and realistic boundary conditions. We also plan to investigate the scalability of the multiplicative fusion mechanism in higher-resolution three-dimensional simulations, where computational efficiency becomes the primary bottleneck.

Impact Statement

This work aims to advance machine learning for scientific computing, with a particular focus on efficient and general neural operator learning for partial differential equations. The proposed LNF-NO architecture improves the training efficiency and practical applicability of operator-learning models, which has potential impact in areas such as computational physics, engineering design, and computational biology. In particular, problems arising from Poisson–Boltzmann and Poisson–Nernst–Planck models are central to biomolecular electrostatics and ion transport modeling, and more efficient operator surrogates may help accelerate exploratory simulations and parameter studies in these domains.

We do not anticipate any direct negative societal or ethical consequences arising from this work. The methods presented are intended to support scientific research and modeling, and do not introduce new concerns related to misuse, fairness, or safety beyond those commonly associated with numerical simulation and surrogate modeling techniques.

References

- [1] Quarteroni, A., Manzoni, A. & Negri, F. *Reduced Basis Methods for Partial Differential Equations: An Introduction*. (Springer, Cham, 2015).
- [2] Benner, P., Gugercin, S. & Willcox, K. A survey of projection-based model reduction methods for parametric dynamical systems. *SIAM Rev.* 57, 483–531 (2015).
- [3] Willcox, K. & Peraire, J. Balanced model reduction via the proper orthogonal decomposition. *AIAA J.* 40, 2323–2330 (2002).
- [4] Lu, L., Jin, P., Pang, G., Zhang, Z. & Karniadakis, G. E. Learning nonlinear operators via DeepONet based on the universal approximation theorem of operators. *Nat. Mach. Intell.* 3, 218–229 (2021).
- [5] Kovachki, N., Li, Z., Liu, B., Azizzadenesheli, K., Bhattacharya, K., Stuart, A. & Anandkumar, A. Neural operator: Learning maps between function spaces. *J. Mach. Learn. Res.* 24, 1–97 (2023).
- [6] Li, Z., Kovachki, N., Azizzadenesheli, K., Liu, B., Bhattacharya, K., Stuart, A. & Anandkumar, A. Fourier neural operator for parametric partial differential equations. In *Int. Conf. Learn. Represent. (ICLR)* (2021).
- [7] Li, Z., Kovachki, N., Choy, C., Li, B., Kossaifi, J. et al. Geometry-informed neural operator for large-scale 3D PDEs. In *Adv. Neural Inf. Process. Syst. (NeurIPS)* 36 (2023).
- [8] Rahman, M. A., Ross, Z. E. & Azizzadenesheli, K. U-NO: U-shaped neural operators. *Trans. Mach. Learn. Res.* (2023).
- [9] Ye, Z., Huang, X., Chen, L., Liu, H., Wang, Z. & Dong, B. PDEformer: Towards a foundation model for one-dimensional partial differential equations. In *ICLR Workshop AI Differ. Equat. Sci.* (2024).
- [10] Perez, E., Strub, F., De Vries, H., Dumoulin, V. & Courville, A. FiLM: Visual reasoning with a general conditioning layer. In *Proc. AAAI Conf. Artif. Intell.* 32 (2018).
- [11] Vaswani, A., Shazeer, N., Parmar, N., Uszkoreit, J., Jones, L., Gomez, A. N., Kaiser, L. & Polosukhin, I. Attention is all you need. *Adv. Neural Inf. Process. Syst.* 30 (2017).
- [12] Shazeer, N., Mirhoseini, A., Maziarz, K., Davis, A., Le, Q. V., Hinton, G. E. & Dean, J. Outrageously large neural networks: The sparsely-gated mixture-of-experts layer. In *Int. Conf. Learn. Represent. (ICLR)* (2017).
- [13] Lu, B., Zhou, Y., Holst, M. J. & McCammon, J. A. Recent progress in numerical methods for the Poisson–Boltzmann equation in biophysical applications. *Commun. Comput. Phys.* 3, 973–1009 (2008).
- [14] Zhang, Q., Gui, S., Li, H. & Lu, B. Model reduction-based initialization methods for solving the Poisson–Nernst–Planck equations in three-dimensional ion channel simulations. *J. Comput. Phys.* 419, 109627 (2020).
- [15] He, K., Zhang, X., Ren, S. & Sun, J. Deep residual learning for image recognition. In *Proc. IEEE Conf. Comput. Vis. Pattern Recognit. (CVPR)* 770–778 (2016).
- [16] Cybenko, G. Approximation by superpositions of a sigmoidal function. *Math. Control. Signals Syst.* 2, 303–314 (1989).
- [17] Hornik, K. Approximation capabilities of multilayer feedforward networks. *Neural Networks* 4, 251–257 (1991).
- [18] Loshchilov, I. & Hutter, F. Decoupled weight decay regularization. In *Int. Conf. Learn. Represent. (ICLR)* (2019).

- [19] Wu, H. & Lu, B. Mathematical artificial data for operator learning. *arXiv preprint arXiv:2507.06752* (2025).
- [20] Jin, P., Meng, S. & Lu, L. MIONet: Learning multiple-input operators via tensor product. *SIAM J. Sci. Comput.* 44, A3490–A3514 (2022).

A Dataset generation and preprocessing

We provide detailed descriptions of the data generation process for each benchmark. Specific numerical parameters are detailed below, and exact reproduction scripts are available in the anonymized supplementary material.

A.1 Laplace dataset generation

We consider the 2D Laplace equation

$$\Delta u = 0 \quad \text{in } \Omega = [0, 1]^2, \quad u|_{\partial\Omega} = g, \quad (8)$$

and learn the solution operator mapping the Dirichlet boundary trace g to the solution field u on a fixed grid. This dataset is generated following the Mathematical Artificial Data (MAD) framework proposed by [19].

Discretization. We use a uniform $N \times N$ grid on Ω with $N = 51$ and spacing $h = 1/(N - 1)$, resulting in $N_g = N^2 = 2601$ evaluation points. The boundary trace is sampled on $\partial\Omega$ using N points per side with duplicated corner points removed, yielding $N_b = 4(N - 1) = 200$ boundary samples. The boundary points are ordered by concatenating the four edges in a fixed counterclockwise manner.

MAD solution family. For each sample, we synthesize a harmonic function as a linear combination of fundamental solutions with sources located outside the domain. Specifically, we draw $J = 10$ source points $\{c_j\}_{j=1}^J$ outside an expanded box $[-\varepsilon, 1 + \varepsilon]^2$ with $\varepsilon = 10^{-3}$, and random weights $\{w_j\}_{j=1}^J$. The solution is defined by

$$u(x) = \sum_{j=1}^J w_j \cdot \frac{1}{2} \log(\|x - c_j\|^2), \quad (9)$$

which is harmonic inside Ω because all sources lie outside Ω .

Data format and normalization. Each sample is stored as a single vector

$$[u_b; u] \in \mathbb{R}^{N_b + N_g},$$

where u_b contains boundary values evaluated at the N_b boundary points and u contains the solution values on the N_g grid points. We apply per-sample normalization by dividing the entire vector by its maximum absolute value so that $\max\| [u_b; u] \| = 1$.

A.2 Burgers dataset generation

We consider the one-dimensional viscous Burgers equation on a periodic domain,

$$\partial_t u(x, t) + u(x, t) \partial_x u(x, t) = \nu \partial_{xx} u(x, t), \quad x \in [0, 2\pi), \quad t \in [0, T], \quad (10)$$

with periodic boundary conditions and viscosity $\nu = 0.01$. The learning task is to approximate the solution operator mapping the initial condition $u_0(x) = u(x, 0)$ to the solution field $u(x, t)$ for $t > 0$.

Initial condition sampling. Initial conditions are generated as low-frequency random Fourier series,

$$u_0(x) = \sum_{m=1}^K \frac{a_m \cos(mx) + b_m \sin(mx)}{m^\alpha}, \quad (11)$$

where $a_m, b_m \sim \mathcal{N}(0, 1)$ are independent standard Gaussian variables, $K = 8$ controls the maximum frequency, and $\alpha = 2.0$ controls spectral decay. Each realization is shifted to have zero mean and normalized to unit standard deviation.

Numerical integration. The Burgers equation is integrated on a fine spatial grid ($N_{\text{fine}} = 512$) using a Fourier spectral method combined with an exponential time-differencing fourth-order Runge–Kutta (ET-DRK4) scheme. A 2/3 dealiasing rule is applied in Fourier space to avoid aliasing errors. The solution is evolved up to final time $T = 1.0$ with time step $\Delta t = 10^{-4}$.

Downsampling and dataset construction. To obtain training data on a coarse grid, the high-resolution solution is low-pass filtered in Fourier space and then downsampled to $N_x = 64$ spatial points. The solution is recorded at $N_t = 100$ uniformly spaced time snapshots (excluding $t = 0$). Each dataset sample therefore consists of the coarse-grid initial condition $u_0 \in \mathbb{R}^{64}$ and the solution trajectory $u \in \mathbb{R}^{64 \times 100}$. The total dataset size is 2000 samples.

A.3 Darcy flow datasets

We consider two Darcy flow benchmarks with different regularity properties of the permeability field: a discontinuous-coefficient dataset obtained from a publicly released benchmark, and a continuous-coefficient dataset generated synthetically by us.

Discontinuous permeability (public dataset). For the discontinuous-permeability benchmark, we use a publicly released Darcy dataset that has been widely adopted in the neural operator and Fourier Neural Operator (FNO) literature. The dataset consists of paired permeability fields $a(x, y)$ with sharp discontinuities and corresponding solutions $u(x, y)$ of the elliptic problem

$$-\nabla \cdot (a(x, y) \nabla u(x, y)) = 1 \quad \text{in } (0, 1)^2, \quad u = 0 \quad \text{on } \partial(0, 1)^2.$$

The data are provided on a uniform grid of resolution 241×241 and distributed in MATLAB format. We utilize the benchmark dataset originally introduced by [6]. Specifically, we obtain the data files from the public repository `raj-brown/fourier_neural_operator`¹ and use them directly without further modification.

Continuous permeability (synthetic dataset). For the continuous-permeability benchmark, we generate the dataset synthetically using the following procedure.

Coefficient generation. The permeability field $a(x, y)$ is generated by evaluating a randomly initialized sinusoidal multilayer perceptron on a uniform grid. Specifically, we use a fully connected network of architecture [2, 50, 50, 1] with sine activations,

$$a_{\text{raw}}(x, y) = W_3 \sin(W_2 \sin(W_1[x, y]^\top + b_1) + b_2) + b_3,$$

and map it to a strictly positive coefficient via $a(x, y) = 0.1 + \text{softplus}(a_{\text{raw}}(x, y))$. The network weights are sampled independently for each realization.

High-resolution PDE solve. Given $a(x, y)$, we solve the Darcy equation on a high-resolution grid of size 241×241 using a finite-difference discretization with face-averaged coefficients and a sparse direct solver.

Downsampling. Both the coefficient field $a(x, y)$ and the solution $u(x, y)$ are downsampled to a 129×129 grid using bilinear interpolation.

A.4 Poisson–Boltzmann (PB) datasets

All PB datasets follow the task definition in Eq. (5):

$$-\Delta u + k \sinh(u) = f \quad \text{in } \Omega, \quad u|_{\partial\Omega} = g, \tag{12}$$

where $k > 0$ partially controls the strength of the nonlinearity. The *PB with source* case corresponds to $f \neq 0$, while other PB cases use $f = 0$.

¹https://github.com/raj-brown/fourier_neural_operator

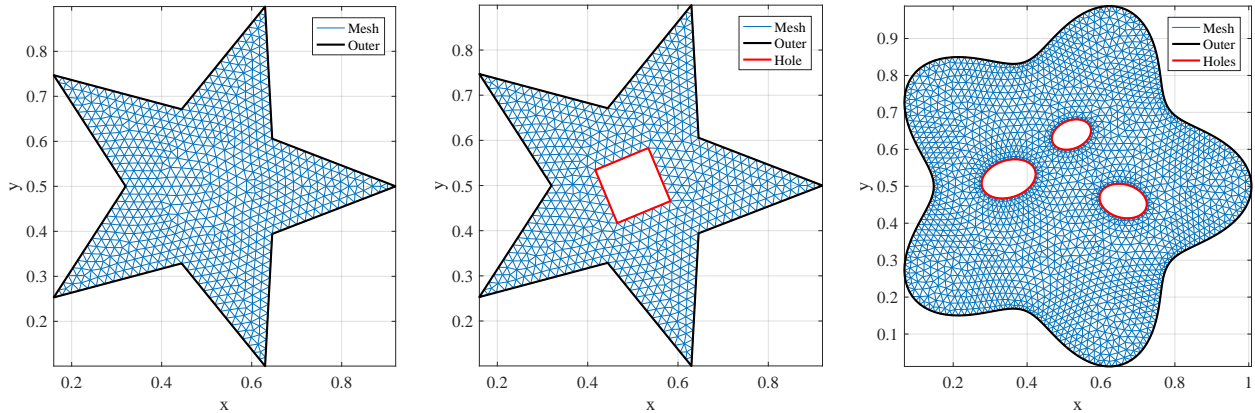


Fig. A1: Representative geometries and corresponding finite-element meshes for the irregular-domain Poisson–Boltzmann benchmarks.

A.4.1 PB on unit square without source

We consider the source-free case $f = 0$ on $\Omega = (0, 1)^2$. The domain is discretized by a uniform $N \times N$ grid ($N = 101$) using the finite difference method (5-point stencil). Boundary values g are sampled on $\partial\Omega$ ($N_b = 400$) and generated as a mixture of low-frequency and high-frequency Gaussian random fields. The resulting discrete nonlinear system is solved using a continuation (homotopy) strategy coupled with a Newton–Raphson method, utilizing a direct sparse solver for the linearized steps. Each accepted realization is stored as a vector $[g; u] \in \mathbb{R}^{N_b + N^2}$.

A.4.2 PB on unit square with source (MAD dataset)

We also consider a source-driven PB dataset following the MAD paradigm [19]. For each sample, we synthesize a smooth field $u(x, y)$ via a randomized sine network and compute the consistent forcing $\tilde{f}(x, y) = \Delta u - k \sinh(u)$. Each sample is stored as $[u_b; \tilde{f}; u]$, where inputs are the boundary trace u_b and the forcing term \tilde{f} .

A.4.3 Irregular-domain PB datasets

To evaluate geometric generalization, we generate PB datasets on irregular planar domains using finite-element methods (FEM). Unlike grid-based datasets, these are *node-based*: solutions are stored at FEM mesh nodes.

Geometry and Solver. We generate three benchmarks: (1) a star-shaped polygon, (2) a star with a square hole, and (3) a flower shape with elliptical holes (see Fig. A1). For each geometry, we generate a fixed triangular mesh. Boundary values are sampled from a periodic Gaussian random field and mapped to boundary nodes. The nonlinear system is solved using linear (P1) finite elements on the unstructured mesh. To ensure robust convergence, we employ a homotopy continuation strategy coupled with a damped Newton–Raphson solver. Within each continuation step, the solution is initialized via Picard iterations, and the linearized systems are solved using a direct sparse solver.

A.4.4 3D PB on unit cube

We generate a 3D dataset on $\Omega = [0, 1]^3$ with $k = 1.0$. The domain is discretized into a $33 \times 33 \times 33$ grid ($N_g = 35937$). Dirichlet boundary conditions are sampled on the 6 faces of the cube, resulting in $N_b = 6N^2 - 12N + 8$ unique boundary points. Inputs g are synthesized using random Yukawa potential sources placed outside the domain to ensure smooth but non-trivial boundary patterns. The nonlinear

system is solved using a finite-difference discretization combined with a damped Newton–Raphson method, where the linearized systems are solved using a direct sparse solver. The dataset consists of 2000 samples.

A.5 Navier–Stokes dataset generation

Governing Equations. We consider the 2D incompressible Navier–Stokes equations on the periodic torus $\mathbb{T}^2 = [0, 1]^2$ in the vorticity–streamfunction formulation. The system governs the evolution of the vorticity field $\omega(x, y, t)$ via:

$$\partial_t \omega + \mathbf{u} \cdot \nabla \omega = \nu \Delta \omega + f(x, y), \quad (13)$$

$$\mathbf{u} = \nabla^\perp \psi = \left(\frac{\partial \psi}{\partial y}, -\frac{\partial \psi}{\partial x} \right), \quad \Delta \psi = \omega, \quad (14)$$

where $\nu = 10^{-3}$ is the viscosity. The streamfunction ψ implicitly enforces the incompressibility condition $\nabla \cdot \mathbf{u} = 0$. The task is to map the initial vorticity $\omega(\cdot, 0)$ to the full trajectory $\omega(\cdot, t)$ for $t \in (0, T]$.

Solver Details. Data is generated using a pseudo-spectral method on a 64×64 uniform grid. Velocity \mathbf{u} is recovered from vorticity ω in the spectral domain via the Poisson equation (14). Time integration uses a Crank–Nicolson scheme for the viscous term and explicit handling of the nonlinear advection term with a time step $\Delta t = 10^{-4}$. We apply the **2/3 rule** for de-aliasing the nonlinear convolution. A deterministic forcing term drives the system:

$$f(x, y) = 0.1 (\sin(2\pi(x + y)) + \cos(2\pi(x + y))).$$

Initial conditions ω_0 are sampled from a Gaussian random field (GRF) with spectral decay $\alpha = 2.5$, length scale $\tau = 7$, and periodic boundaries. We simulate up to $T = 50$ and record $N_t = 50$ snapshots (i.e., at unit time intervals) for training.

A.6 Poisson–Nernst–Planck (PNP) dataset generation

Governing Equations. For operator-learning benchmarking, we consider the dimensionless steady-state Poisson–Nernst–Planck system for a binary symmetric electrolyte. The system describes the coupling between the electrostatic potential ϕ and the ionic concentrations c_\pm (see, e.g., [14] for formulation details), governed by the following equations:

$$-\Delta \phi = c_+ - c_-, \quad \nabla \cdot (\nabla c_\pm \pm c_\pm \nabla \phi) = 0, \quad (15)$$

where the domain is the unit square $\Omega = (0, 1)^2$. The first equation (Poisson) relates the potential to the charge density difference, while the second pair (Nernst–Planck) describes the conservation of mass under diffusion and electromigration. This formulation captures the essential nonlinear coupling where potential gradients drive ion transport and ion distributions determine the potential field.

Solver & Data. We generate the reference solutions using a Gummel fixed-point iteration scheme. At each iteration step, the Poisson equation and the Nernst–Planck equations are solved sequentially using finite differences on a 129×129 uniform grid until convergence. The input boundary conditions are generated via truncated Fourier series, with strictly enforced positivity ($c_\pm > 0$) to ensure physical validity. The final dataset consists of 2000 samples, mapping the three boundary traces (g_ϕ, g_{c_+}, g_{c_-}) to the full interior fields (ϕ, c_+, c_-).

B Training and evaluation protocol

Hardware and software. Experiments are conducted on a single NVIDIA GeForce RTX 4070 Laptop GPU using PyTorch 2.4.1. Wall-clock training time excludes data generation.

Data split and Normalization. We use a fixed 9:1 train/test split. All inputs and outputs are normalized using global statistics (mean and standard deviation) computed strictly on the training set. Evaluation is always performed on the *physical scale* by decoding predictions back to the original domain.

Loss functions. For scalar fields, we use the relative L^2 error:

$$\text{rel } L^2(\hat{u}, u) = \frac{\|\hat{u} - u\|_2}{\|u\|_2 + \varepsilon}, \quad \varepsilon = 10^{-12}.$$

For the coupled PNP task, we use the mean of the relative errors of the three fields (ϕ, c_+, c_-) .

Optimization. We use the AdamW optimizer with weight decay 10^{-4} (excluding bias and scale parameters). We employ a constant learning rate (no decay) for 500 epochs. Batch sizes are set to 20 or 32 depending on GPU memory constraints.

Reproducibility. Due to computational constraints and to facilitate reproducibility, our main results are reported using a single fixed random seed. Our preliminary checks on PB $k = 1$ across seeds $\{0, \dots, 4\}$ suggest that the model is generally robust to seed choice: four runs yield closely clustered errors ($\approx 2.3\text{--}2.6 \times 10^{-2}$), with one outlier seed producing a larger error.

Supplementary code. An anonymized implementation used in our experiments is provided as supplementary material.

C LNF-NO architecture details

We categorize the architectures based on their input-output configurations: **Single-Input Single-Output (SISO)**, mapping a single functional input to a single output field; **Multiple-Input Single-Output (MISO)**, processing multiple functional inputs to predict a single output field; and **Multiple-Input Multiple-Output (MIMO)**, processing multiple functional inputs to predict multiple coupled output fields.

All LNF-NO variants share the same multiplicative fusion structure:

$$\hat{y} = \alpha(\mathcal{B}_L(z) \odot \mathcal{B}_N(z)),$$

where an encoder maps the input to latent features z , and α is a learned scalar. The linear branch \mathcal{B}_L is a pure linear map (affine transformation), while the nonlinear branch \mathcal{B}_N uses `tanh` activations.

C.1 Architecture Configurations

(A) Regular-domain SISO (Laplace, PB). Input: Boundary $g \in \mathbb{R}^{N_b}$. Output: Grid $u \in \mathbb{R}^{N^2}$.

- **Encoder (1D CNN):** Four layers.
 - Conv1d(1, 64, k=9, s=1, p=4)
 - Three layers of Conv1d(64, 64, k=9, s=2, p=4)
- **Branches (MLP):** Feature dim d to grid dim $D = N^2$.
 - \mathcal{B}_L : Linear $[d \rightarrow 256 \rightarrow D]$. Note that while mathematically equivalent to a single linear map, the two-layer structure (without intermediate activation) is maintained to align the latent width with the nonlinear branch for elementwise fusion and to provide additional optimization degrees of freedom.
 - \mathcal{B}_N : MLP $[d \rightarrow 256 \rightarrow 256 \rightarrow D]$.

- **Decoder (2D CNN):**
 - Conv2d(1, 32, k=3, s=1, p=1)
 - Conv2d(32, 32, k=3, s=1, p=1)
 - Conv2d(32, 1, k=3, s=1, p=1)

(B) **Regular-domain MISO (PB-Source).** Input: Boundary g and Source f . Output: Grid u .

- **Encoders:**
 - Boundary: Same as (A).
 - Source: Four-layer 2D CNN (channels $1 \rightarrow 32$, stride 2) followed by Adaptive Avg Pool to 8×8 .
- **Branches & Decoder:** Identical to (A).

(C) **Irregular-domain SISO (PB-FEM).** Input: Boundary g . Output: Node vector $u \in \mathbb{R}^{N_p}$.

- **Encoder:** Same 1D boundary encoder as (A).
- **Branches:** Output dimension $D = N_p$ (mesh nodes).
 - \mathcal{B}_L : Linear [$d \rightarrow 256 \rightarrow D$].
 - \mathcal{B}_N : MLP [$d \rightarrow 256 \rightarrow 256 \rightarrow D$].
- **Decoder:** None (direct node prediction).

(D) **Regular-domain MIMO (PNP).** Input: 3 Boundaries. Output: 3 Fields.

- **Encoders:** Three independent 1D encoders (same architecture as A).
- **Branches:** Output dim $D = 3N_xN_y$.
- **Decoder:** 3-channel 2D CNN (3->64->64->3).

(E) **3D Poisson–Boltzmann (Regular-domain SISO).** Input: Boundary $g \in \mathbb{R}^{N_b}$. Output: Grid $u \in \mathbb{R}^{N^3}$ ($N = 33$). Unlike the 2D cases, we omit the explicit 1D encoder for the boundary vector to reduce memory overhead, passing g directly to the branches.

- **Branches (MLP):** Map input dimension N_b directly to grid dimension $D = N^3$.
 - \mathcal{B}_L : Linear projection [$N_b \rightarrow 256 \rightarrow D$].
 - \mathcal{B}_N : MLP [$N_b \rightarrow 256 \rightarrow 256 \rightarrow D$] with **tanh** activations.
- **Decoder (3D CNN):**
 - Conv3d(1, 32, k=3, s=1, p=1)
 - Conv3d(32, 32, k=3, s=1, p=1)
 - Conv3d(32, 1, k=3, s=1, p=1)

D Ablation Studies

Setup. We conduct ablation studies on the regular-domain Poisson–Boltzmann (PB) benchmark with $k = 1$ to isolate the roles of (i) the encoder, (ii) the decoder, and (iii) the linear–nonlinear multiplicative fusion in LNF-NO.

Variants. We consider the following model variants:

- **Full (LNF-NO):** Encoder + Linear \odot Nonlinear + Decoder.
- **Only Nonlinear branch:** Remove the linear branch (retaining encoder/decoder).
- **Only Linear branch:** Remove the nonlinear branch (retaining encoder/decoder).
- **w/o Encoder:** Remove the 1D convolutional encoder.
- **w/o Decoder:** Remove the 2D convolutional decoder.
- **w/o Encoder & Decoder:** Pure multiplicative MLP.
- **Pure Nonlinear MLP:** Only the nonlinear branch, no encoder/decoder.
- **Pure Linear MLP:** Only the linear branch, no encoder/decoder.

Here, “w/o” denotes “without” for brevity in Table A1.

Results. Table A1 summarizes the parameter count, training time, and test relative L^2 error.

Model	#Params	Epochs	Time (s)	Test Rel. L^2
Full (LNF-NO)	7,069,300	500	465.43	2.29e-02
Only Nonlinear branch	3,628,187	500	386.68	5.10e-02
Only Linear branch	3,562,395	500	394.70	2.15e-02
w/o Encoder	5,524,276	500	377.32	3.60e-02
w/o Decoder	7,059,443	500	164.86	2.94e-02
w/o Enc & Dec	5,514,419	500	105.50	7.30e-02
Pure Nonlinear MLP	2,790,106	500	70.11	8.39e-02
Pure Linear MLP	4,090,602	500	70.28	1.97e-01

Table A1: Ablation results on the PB ($k = 1$) benchmark.

Discussion.

- **Role of encoder/decoder.** Removing both encoder and decoder causes a large performance drop (7.30e-02), indicating that convolutional modules provide essential structural inductive bias.
- **Linear branch with convolutions.** The “Only Linear branch” variant achieves comparable performance to the full model (2.15e-02 vs. 2.29e-02), suggesting that a substantial portion of the expressivity arises from the convolutional feature extractor combined with a global linear mapping.
- **Multiplicative fusion.** While not strictly necessary for this specific PB regime, the multiplicative fusion improves robustness and becomes more beneficial in strongly nonlinear settings (cf. Table 3 in the main text).
- **Pure linear is insufficient.** A purely linear model without convolution performs poorly (1.97e-01), confirming that the operator cannot be well-approximated by a global linear mapping alone.

E Baselines

To benchmark the performance of LNF-NO, we compare it against two established operator learning pillars: the Deep Operator Network (DeepONet) [4] and the Fourier Neural Operator (FNO) [6]. The hyperparameters selected for the baselines (e.g., basis dimension p and frequency modes k_{\max}) align with standard configurations widely used in the community to ensure a fair comparison. All baseline models are trained using the same rigorous protocol as LNF-NO:

- **Data Split:** A fixed 9:1 training-to-testing ratio is used for all datasets.
- **Normalization:** Inputs and outputs are normalized using global statistics computed strictly on the training set.
- **Metrics:** All reported errors are relative L^2 norms computed on the decoded physical scale after inverse normalization.
- **Optimization:** We use the AdamW optimizer with bias terms excluded from weight decay. No learning rate decay (constant LR) is applied.

DeepONet models are trained with a larger epoch budget (scaled by $10\times$) and a lower learning rate ($10^{-1}\times$) compared to FNO and LNF-NO, reflecting the architecture’s different convergence characteristics.

E.1 Deep Operator Network (DeepONet)

We employ the unstacked DeepONet architecture, which approximates the operator \mathcal{G} by taking an input function u (via a discrete sensor vector) and a query coordinate y to predict the solution value $\mathcal{G}(u)(y)$. The network consists of two sub-networks: a *Branch Net* encoding the input function and a *Trunk Net* encoding the coordinates. The final prediction is given by the inner product of their outputs (plus an optional bias):

$$\hat{u}(y) = \sum_{k=1}^p b_k(u) \cdot t_k(y) + \beta,$$

where $\{b_k\}_{k=1}^p$ and $\{t_k\}_{k=1}^p$ are the p -dimensional outputs of the branch and trunk networks, respectively. For all tasks, we set the basis dimension to $p = 1024$. The Branch and Trunk networks are implemented as 5-layer MLPs with a hidden width of 256 and `tanh` activations.

(A) Regular-domain SISO (Laplace, PB). The branch net input is the boundary vector $g \in \mathbb{R}^{N_b}$, and the trunk net input is the coordinate $x \in \mathbb{R}^2$.

- Branch: $\text{MLP}(N_b \rightarrow 1024)$ with hidden width 256.
- Trunk: $\text{MLP}(2 \rightarrow 1024)$ with hidden width 256.

For the 3D PB task, the trunk net takes 3D coordinates (x, y, z) as input. The architecture parameters remain consistent ($p = 1024$, width=256).

(B) Regular-domain MISO (PB-Source). For tasks with multiple inputs (boundary $u_b \in \mathbb{R}^{N_b}$ and source $f \in \mathbb{R}^{N^2}$), we employ a multi-branch fusion strategy (similar to MIONet [20]). Separate branch nets encode u_b and f , and their embeddings are fused via elementwise multiplication before the dot product with the trunk:

$$b(u_b, f) = b^{(u)}(u_b) \odot b^{(f)}(f) \in \mathbb{R}^p.$$

- Branch 1: $\text{MLP}(N_b \rightarrow 1024)$.
- Branch 2: $\text{MLP}(N^2 \rightarrow 1024)$.
- Trunk: $\text{MLP}(2 \rightarrow 1024)$.

(C) Regular-domain MIMO (PNP). For the coupled PNP system, we use a single concatenated branch net. The trunk net is modified to have three separate output heads to predict the three fields (ϕ, c_+, c_-) simultaneously:

$$\hat{u}^{(m)}(x) = \sum_{k=1}^p b_k(\mathbf{u}_{bc}) \cdot t_k^{(m)}(x), \quad m \in \{\phi, c_+, c_-\}.$$

- Branch: MLP($3N_b \rightarrow 1024$).
- Trunk: MLP($2 \rightarrow 3 \times 1024$).

E.2 Fourier Neural Operator (FNO)

We adopt the standard Fourier Neural Operator architecture. The model processes the input $a(x)$ through three main stages:

1. **Encoder (Lifting):** The input is projected pointwise to a high-dimensional channel space $v_0(x) \in \mathbb{R}^{d_h}$ via a linear layer or shallow MLP.
2. **Fourier Integral Layers:** The latent representation is updated through a sequence of L layers. The update rule for the l -th layer is:

$$v_{l+1}(x) = \sigma(W_l v_l(x) + (\mathcal{F}^{-1} \circ R_l \circ \mathcal{F})(v_l)(x)),$$

where σ is a nonlinear activation function, W_l is a pointwise linear transform (residual connection), \mathcal{F} denotes the FFT, and R_l is a learnable complex weight tensor that mixes the lowest k_{\max} frequency modes.

3. **Decoder (Projection):** The final features $v_L(x)$ are mapped to the target dimension using a pointwise MLP decoder.

Input lifting strategy. Since FNO requires grid-structured inputs, strictly lower-dimensional inputs (e.g., boundary conditions) are mapped to the full spatiotemporal grid prior to the lifting stage. We employ standard techniques consistent with the literature: *domain replication* for scalar/vector inputs, *zero-padding* (placing boundary values on the perimeter with zero-filled interiors) for boundary fields, or learned *MLP projection*. The resulting fields are concatenated with coordinate grids.

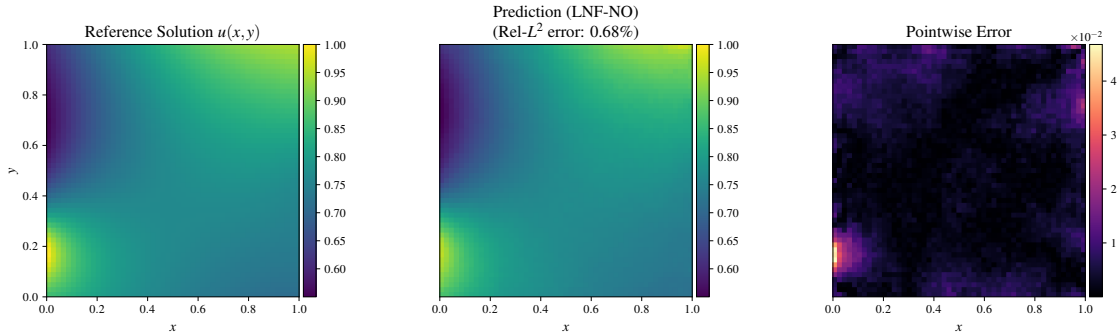
Hyperparameters. We set the network depth to $L = 4$ for all tasks. Consistent with our training protocol, we employ ReLU activation for all FNO baselines. Specific structural parameters are:

- **2D Steady-state (Laplace, PB, Darcy, PNP):** We use a 2D FNO with $k_{\max} = 16$ modes per direction and width $d_h = 64$. The PNP model uses a 5-channel input (via zero-padding) and predicts 3 fields simultaneously.
- **Burgers (1D time-dependent):** Modeled as a 2D FNO on the (x, t) domain. Configuration: $k_{\max} = 16$, $d_h = 64$.
- **Navier–Stokes (2D time-dependent):** Modeled as a 3D FNO on the (x, y, t) domain. Input consists of $T_{\text{in}} = 10$ history frames stacked with coordinates. Configuration: $k_{\max} = 12$, $d_h = 20$.
- **3D Poisson–Boltzmann:** Modeled as a 3D FNO on the (x, y, z) domain. Configuration: $k_{\max} = 8$ modes per direction, width $d_h = 32$.

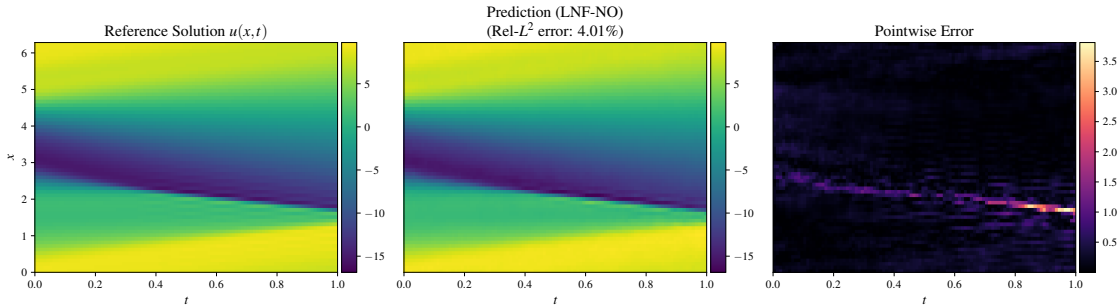
F Visualization of predictions

In this section, we provide qualitative visualizations of the LNF-NO predictions on unseen test samples. Unless otherwise stated, the columns display: (1) The **Reference Solution** (Ground Truth) obtained from the numerical solver; (2) The **Prediction** output by our LNF-NO model; (3) The pointwise **Absolute Error** map ($|u - \hat{u}|$). For tasks with spatially varying coefficients or source terms, the input field is also visualized in the first column.

Note: Visualizations for the 3D Poisson–Boltzmann benchmark are presented in the main text (see the corresponding Figure 2) and are therefore omitted here to avoid redundancy.



(a) **Laplace Equation:** Prediction of the harmonic function on a regular grid.



(b) **Burgers Equation:** A snapshot of the wave propagation. The model sharply resolves the shock front with minimal oscillation.

Fig. A2: Standard Benchmarks. Visualizations for (a) the steady-state 2D Laplace equation and (b) the time-dependent 1D Burgers equation.

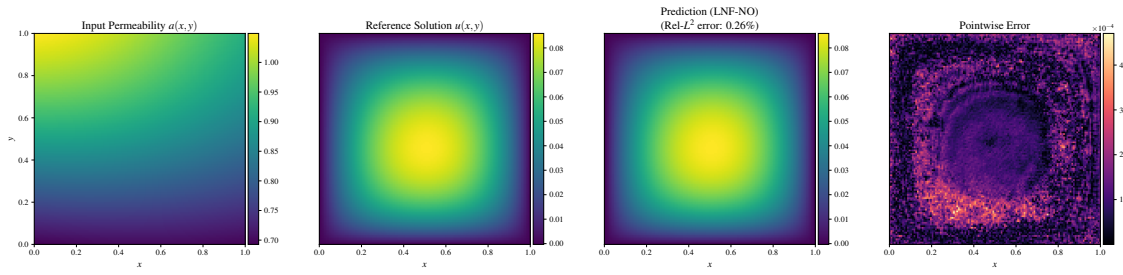


Fig. A3: Darcy Flow (Continuous Coefficients). From left to right: Input Permeability $a(x, y)$, Reference Solution $u(x, y)$, Prediction, and Absolute Error.

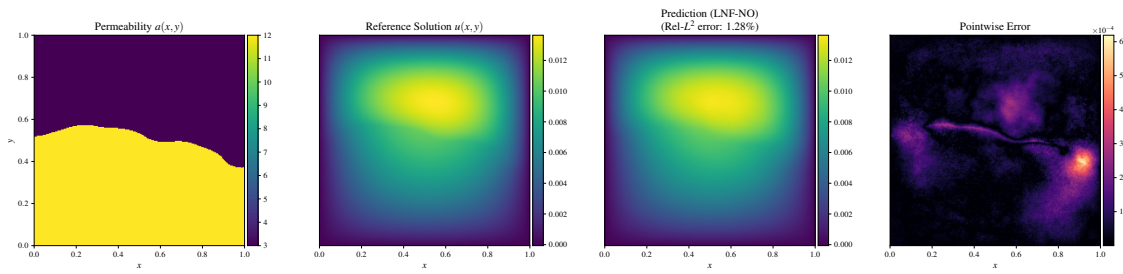


Fig. A4: Darcy Flow (Discontinuous Coefficients). The model effectively handles sharp transitions in the solution field caused by jump coefficients.

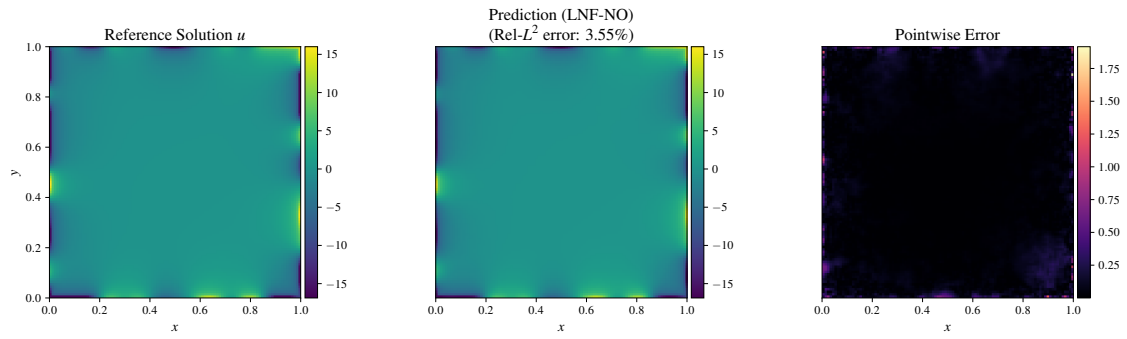


Fig. A5: Poisson–Boltzmann (High Nonlinearity $k = 100$). The model captures the sharp boundary layers induced by the strong sinh nonlinearity.

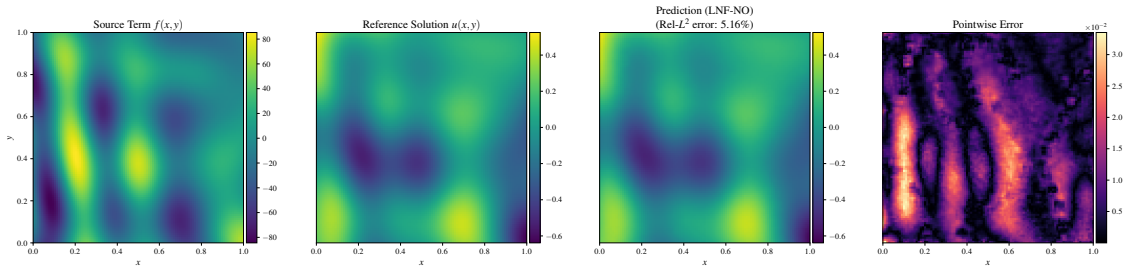


Fig. A6: Poisson–Boltzmann (Source-Driven). Includes the variable source term $f(x, y)$ (first column) as input.

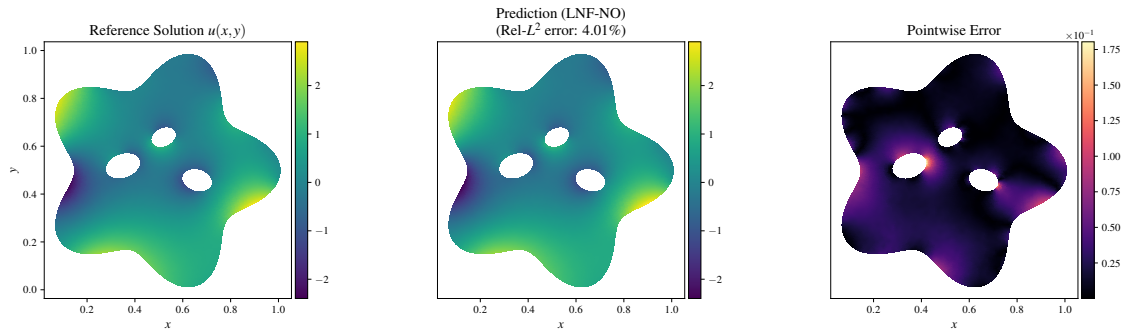


Fig. A7: Geometric Generalization (Irregular PB). Predictions on complex non-simply-connected domains, including the “Flower” shape with elliptical holes. Since this task uses the node-based architecture, results are plotted directly on the finite-element mesh triangulation. LNF-NO accurately captures the solution field along the intricate curved boundaries, confirming its capability to handle unstructured data and complex topologies without regular grid interpolation.

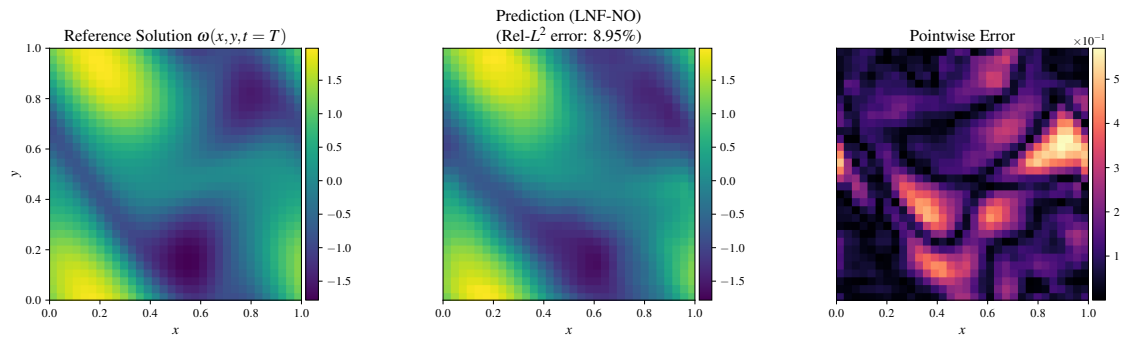


Fig. A8: Navier–Stokes Equation. Prediction of the vorticity field $\omega(x,y,t)$ at the final time step $T = 50$. The model successfully tracks the evolution of complex vortex structures and turbulent features over long time horizons.

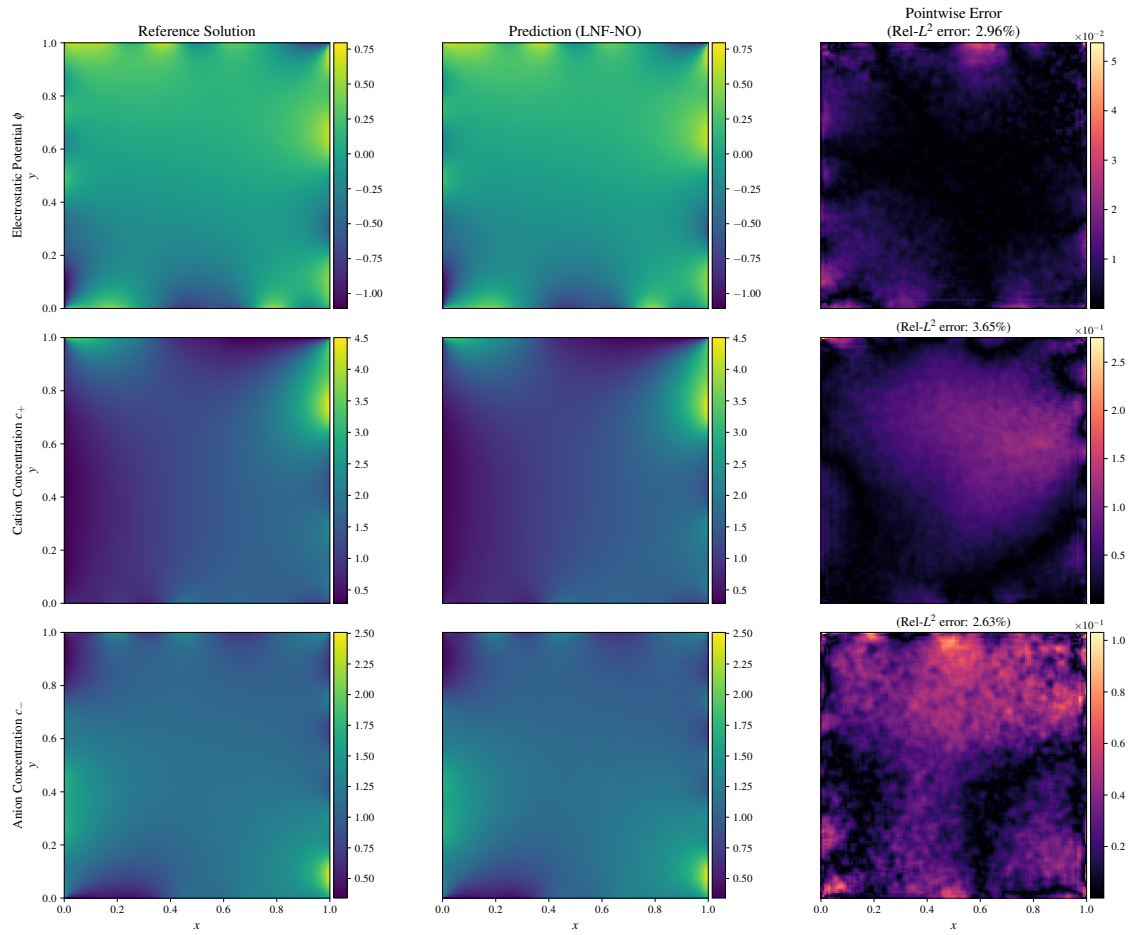


Fig. A9: Poisson–Nernst–Planck (PNP) System. Simultaneous prediction of three strongly coupled fields: Electrostatic Potential ϕ (top), Cation Concentration c_+ (middle), and Anion Concentration c_- (bottom). The input boundary conditions (not shown) drive complex internal distributions. The error maps (right column) demonstrate that LNF-NO maintains physical consistency across the variables and accurately resolves the sharp concentration gradients (Debye layers) near the boundaries, which are typical in electro-diffusion problems.